

Crystallographically Textured Nanomaterials

Produced from the Liquid Phase Sintering of $\text{Bi}_x\text{Sb}_{2-x}\text{Te}_3$ Nanocrystal Building Blocks

*Yu Liu,[†] Yu Zhang,[†] Silvia Ortega,[†] Maria Ibáñez,^{‡,§} Khak Ho Lim,[⊥] Albert Grau-Carbonell,^{//}
Sara Martí-Sánchez,^{//} Ka Ming Ng,[⊥] Jordi Arbiol,^{//,#} Maksym V. Kovalenko,^{‡,§} Doris
Cadavid,^{†,¶,*} and Andreu Cabot^{†,#,*}*

[†] Catalonia Energy Research Institute - IREC, Sant Adria de Besòs, 08930 Barcelona, Spain.

[‡] Institute of Inorganic Chemistry, Department of Chemistry and Applied Biosciences, ETH Zürich, Vladimir Prelog Weg 1, CH-8093, Switzerland.

[§] Empa-Swiss Federal Laboratories for Materials Science and Technology, Dübendorf, Überlandstrasse 129, CH-8600, Switzerland.

[⊥] Department of Chemical and Biological Engineering, Hong Kong University of Science and Technology, Hong Kong, China.

^{//} Catalan Institute of Nanoscience and Nanotechnology (ICN2), CSIC and BIST, Campus UAB, Bellaterra, 08193 Barcelona, Catalonia, Spain.

[#] ICREA, Pg. Lluís Companys 23, 08010 Barcelona, Spain.

[¶] Departamento de Física, Universidad Nacional de Colombia, 111321, Ciudad Universitaria, Bogotá, Colombia.

ABSTRACT: Bottom-up approaches for producing bulk nanomaterials have traditionally lacked control over the crystallographic alignment of nanograins. This limitation has prevented nanocrystal-based nanomaterials from achieving optimized performances in numerous applications. Here we demonstrate the production of nanostructured $\text{Bi}_x\text{Sb}_{2-x}\text{Te}_3$ alloys with controlled stoichiometry and crystallographic texture through proper selection of the starting building blocks and the adjustment of the nanocrystal-to-nanomaterial consolidation process. In particular, we hot pressed disk-shaped $\text{Bi}_x\text{Sb}_{2-x}\text{Te}_3$ nanocrystals and tellurium nanowires as building blocks using multiple pressure and release steps at a temperature above the tellurium melting point. We explain the formation of the textured nanomaterials through a solution-reprecipitation mechanism under a uniaxial pressure. Additionally, we further demonstrate these alloys to reach unprecedented thermoelectric figures of merit, up to $ZT=1.96$ at 420 K, with an average value of $ZT_{\text{ave}}=1.77$ for the record material in the temperature range 320-500 K, thus potentially allowing up to 60 % higher energy conversion efficiencies than commercial materials.

KEYWORDS: $\text{Bi}_x\text{Sb}_{2-x}\text{Te}_3$, nanocrystal, crystal texture, liquid phase sintering, thermoelectric, energy conversion.

Nanostructured materials hold the key to the cost-effective use of thermoelectric devices in a broad range of applications. Nanomaterials are characterized by reduced thermal conductivities attributed to phonon scattering at grain boundaries;^{1, 2} the potential to simultaneously combine high charge carrier concentrations with large charge carrier mobilities through modulation doping;³⁻⁵ and the possibility to maximize the Seebeck coefficient by modifying the electronic band structure or through electron energy filtering at interphases.^{6, 7} However, to optimize all these properties, an exquisite control over nanomaterial parameters in three dimensions is

necessary. Such level of control cannot be reached by current high throughput bulk nanomaterial fabrication technologies, such as mechanical grinding. Alternative vacuum-based thin film technologies are able to produce compositionally tuned films, but with limited thickness and at expenses of high production costs and low throughputs.

Bottom-up assembly strategies that use nanocrystals as starting building blocks allow producing bulk nanomaterials with parameters tuned at the nanometer-scale and in a cost-effective manner. This approach has been successful to produce a plethora of nanocrystalline materials with exceptional thermoelectric properties.^{1, 3, 8-10} However, this methodology faces limitations in the production of highly anisotropic materials with proper crystallographic alignment, as required in numerous application fields, including thermoelectrics.¹

In particular, n-type $\text{Bi}_2\text{Te}_{3-x}\text{Se}_x$ and p-type $\text{Bi}_x\text{Sb}_{2-x}\text{Te}_3$ alloys, the most ubiquitous thermoelectric materials operated at ambient temperature, have layered structures consisting of stacks of covalently bonded quintuple atomic layers, Te-Bi/Sb-Te-Bi/Sb-Te, that are held together by weak van der Waals interactions (Figure S1). Such layered materials are characterized by strongly anisotropic transport properties. In single crystals, the electrical conductivities in the ab plane are higher than in the c direction, up to factors 4.38 and 2.65 for $\text{Bi}_2\text{Te}_{2.6}\text{Se}_{0.4}$ and $\text{Bi}_{0.5}\text{Sb}_{1.5}\text{Te}_3$ respectively.^{11, 12} Similarly, two-fold higher thermal conductivities are measured within the ab plane. Even though the Seebeck coefficient is nearly isotropic, overall, higher thermoelectric figures of merit, up to factors 2.17 and 1.42 for $\text{Bi}_2\text{Te}_{2.6}\text{Se}_{0.4}$ and $\text{Bi}_{0.5}\text{Sb}_{1.5}\text{Te}_3$, are measured in the ab plane when compared with the c direction. Such strong anisotropy requires producing crystallographically textured $\text{Bi}_2\text{Te}_{3-x}\text{Se}_x$ and $\text{Bi}_x\text{Sb}_{2-x}\text{Te}_3$ nanomaterials to optimize their thermoelectric properties.

To generate crystallographically textured polycrystalline materials, severe plastic deformation approaches, such as particular extrusion strategies^{13, 14} and high pressure torsion¹⁵ have been used with some success. More conventional processes, such as hot press and spark plasma sintering, have been also effective in producing $\text{Bi}_2\text{Te}_{3-x}\text{Se}_x$ and $\text{Bi}_x\text{Sb}_{2-x}\text{Te}_3$ polycrystalline materials with significant degrees of crystallographic alignment.¹⁶⁻¹⁸ Combining these methodologies with micropowders produced by ball milling, polycrystalline pellets with relatively thick layered structures, ca. 0.5-1 μm , have been obtained. To optimize such consolidation processes, most parameters have been investigated, but some controversy has arisen. As an example, it is generally assumed that anisotropy is stimulated by severe pressures and temperatures, but in some cases, less orientation at higher processing temperatures have been reported.¹⁷ In other works the size of the die was considered as the main parameter determining the degree of crystallographic texture.¹⁶ Overall, three main conclusions have been generally accepted: i) crystallographically aligned $\text{Bi}_2\text{Te}_{3-x}\text{Se}_x$ and $\text{Bi}_x\text{Sb}_{2-x}\text{Te}_3$ alloys are produced with the c direction oriented along the pressing direction; ii) in such materials, improved thermoelectric properties are measured or assumed within the ab plane when compared with the c direction; and iii) much room is left for improvement through optimizing these processes.

Here, we detail a liquid phase sintering strategy to systematically produce crystallographically textured $\text{Bi}_x\text{Sb}_{2-x}\text{Te}_3$ materials with thin layered structures. We further prove that these nanomaterials are characterized by record thermoelectric figures of merit, although not in the ab plane, but in the c direction.

$\text{Bi}_x\text{Sb}_{2-x}\text{Te}_3$ nanocrystals with controlled composition were used as precursor building blocks to produce bulk nanocrystalline pellets. Figure 1a shows a representative scanning electron microscopy (SEM) micrograph of the disk-shaped $\text{Bi}_x\text{Sb}_{2-x}\text{Te}_3$ nanocrystals produced in

diethylene glycol from bismuth (III) nitrate, antimony (III) chloride and sodium tellurite in the presence of hydrazine and polyvinylpyrrolidone (PVP) at 190 °C (see details in the supporting information, SI). Over 5 g of nanocrystals per batch were produced using this synthetic protocol (Figure S2a). Composition could be easily tuned around its optimum value for thermoelectric applications ($x=0.5$) by adjusting the initial ratios of the bismuth and antimony precursors (Figure 1b and table S2-3). In all samples, excess amounts of tellurium, nominally $\text{Te}/(\text{Bi}+\text{Sb})=1.875$, were introduced in the reaction mixture. The produced nanocrystal ensemble systematically conserved the nominal Bi/Sb ratios and an excess of tellurium: $\text{Te}/(\text{Bi}+\text{Sb})\sim 1.7$. Excess tellurium was found in the form of thin tellurium nanorods, segregated from $\text{Bi}_x\text{Sb}_{2-x}\text{Te}_3$ nanodisks, as pointed out by red arrows in Figure 1a.

$\text{Bi}_x\text{Sb}_{2-x}\text{Te}_3$ nanocrystals were purified by multiple precipitation and redispersion steps (SI). Subsequently, they were dried and annealed at 350 °C for 60 min under argon flow inside a tube furnace to remove remaining organics. The annealed nanopowders still consisted of disk-shaped $\text{Bi}_x\text{Sb}_{2-x}\text{Te}_3$ nanocrystals (Figure 1c and Figure S2b-d), and contained large tellurium nanorods grown during the annealing step from the excess amounts of this element in the original sample, as observed by SEM (Figure 1c) and x-ray diffraction (XRD, Figure 1d).

The annealed nanopowders were hot-pressed for 210 s within an inert atmosphere into cylindrical pellets (10 mm in diameter and 10 mm length) using 80 MPa of pressure. The whole procedure, lasting less than 5 minutes and requiring no vacuum and moderate processing temperatures, resulted in $\text{Bi}_x\text{Sb}_{2-x}\text{Te}_3$ cylinders with relative densities ca. 90% of the theoretical value, as measured by the Archimedes' method. From these cylinders, rectangular bars of about $8\times 6\times 1\text{ mm}^3$ were cut in two directions, along the press axis, i.e. the cylinder length, and within the plane normal to this axis, i.e. the cylinder disk plane (Figure S6).

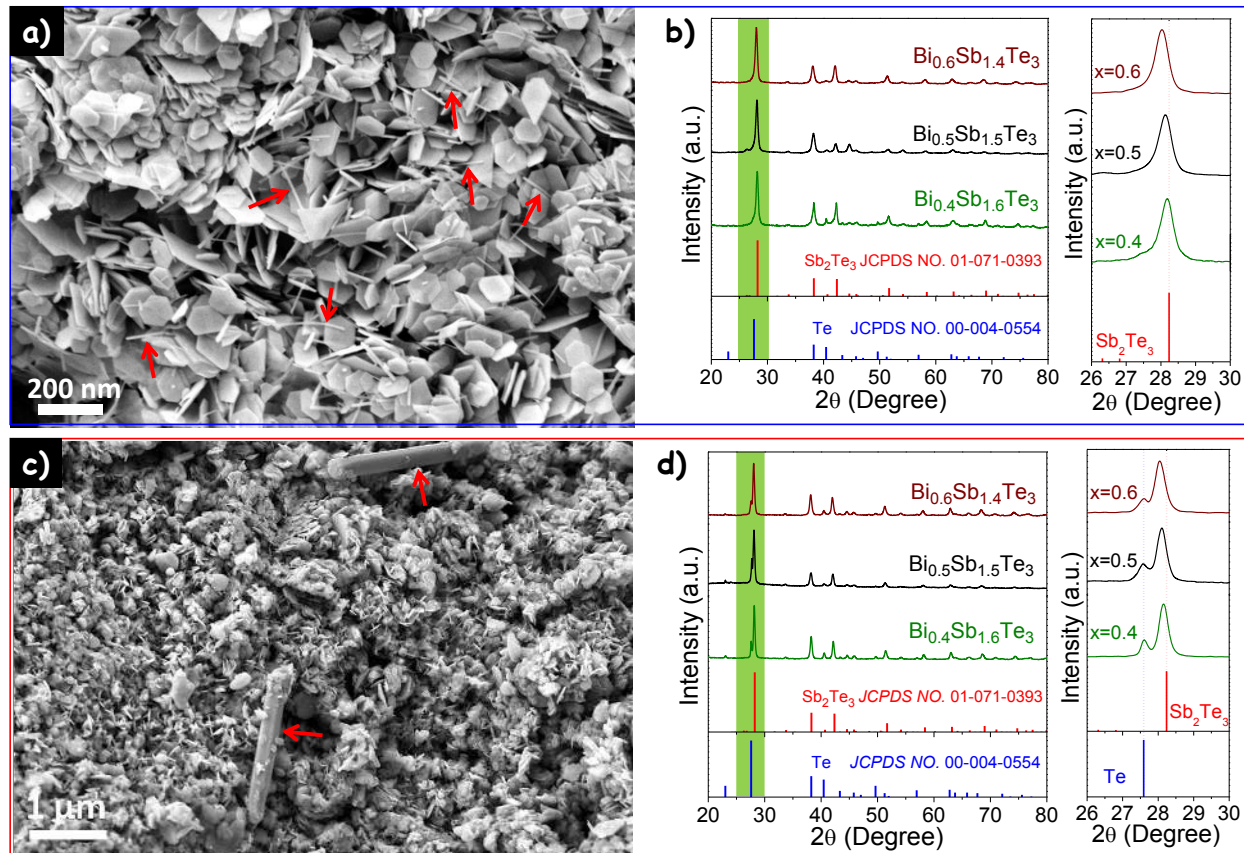


Figure 1. Representative SEM micrographs (a,c) and XRD patterns (b,d) of the $\text{Bi}_x\text{Sb}_{2-x}\text{Te}_3$ disk-shaped nanocrystals used in this work, before (a,b) and after (c,d) annealing. Tellurium nanorods were present in samples prepared with a nominal excess of tellurium and are pointed out by arrows in the SEM images of the sample before and after annealing. The presence of large tellurium nanorods in the annealed sample is also evidenced from the XRD peak at $2\theta=27.6^\circ$.

The uniaxial hot press of the materials at temperatures below 400 °C resulted in relatively isotropic pellets containing small nanograins with random orientations (Figure 2f, g). On the other hand, when hot pressing the annealed nanopowders at temperatures above 450 °C, pellets with strong crystallographic texture, with the [001] crystallographic direction oriented along the press axis, were produced (Figure 2a-d). Figures 2a-2c show top-view and cross-section SEM micrographs of a pellet produced from hot pressing $\text{Bi}_x\text{Sb}_{2-x}\text{Te}_3$ nanodisks at 480 °C. A laminar

structure, with layer thicknesses of around 40 nm and extending several tens and even hundreds of microns in the disk plane, was systematically observed in all the samples produced at this temperature. These layers displayed a homogeneous distribution of Bi and Sb and contained numerous stacking faults as observed from STEM-EELS and HRTEM characterization of a pellet cross-section (Figures S4 and S5). Figures 2d and S3 display the XRD patterns measured in two perpendicular orientations of the cylinder, along and normal to the press axis. The XRD pattern of the pellet held with the press axis normal to the support, showed a clear increase of the diffraction peaks corresponding to the [001] crystallographic directions with respect to the pattern obtained from the cylinder held planar (Figure 2d).

The excess of tellurium in the initial nanopowder was essential to produce highly crystallographically textured nanomaterials (Figure S7). During the hot press process at 480 °C, the excess of tellurium, ca. 8% in volume, liquefied (tellurium melting point is 449.5 °C), creating a solid-liquid interface with two main potential consequences.

The liquid interface reduced the interparticle friction, potentially facilitating the reaccommodation of the solid nanocrystals. In a pure nanocrystal rearrangement scenario, the final pellet would consist of disk-shaped nanocrystals identical to those observed in the precursor nanopowders, but all aligned in one preferential direction dictated by the press axis. However, this was not the observed pellet nanostructure (Figure 2a-c).

The tellurium liquid phase could also dissolve the randomly oriented $\text{Bi}_x\text{Sb}_{2-x}\text{Te}_3$ nanocrystals, allow a fast atomic diffusion of the alloy elements, and feed, when oversaturated, the nucleation and growth of new $\text{Bi}_x\text{Sb}_{2-x}\text{Te}_3$ crystals oriented in a preferential direction dictated by the press axis. In the liquid phase sintering literature, this sintering mechanism is known as the solution-

reprecipitation stage.¹⁹ Indeed, at 480 °C, liquid tellurium can dissolve around 15% of Sb and 25% of Bi. Actually, both the Sb-Te and Bi-Te systems have eutectic points: at 422 °C for Sb-Te with a 7.4% of Sb and at 413 °C with 10% of Bi in the Bi-Te system.^{20, 21} The dissolution of the solid in the liquid phase varies inversely with the crystal size, thus smaller grains and higher energy surfaces preferentially dissolve, contributing to the formation of larger grains. In this Ostwald ripening scenario, randomly oriented small disk-shaped nanocrystals are rapidly dissolved and larger and crystallographically oriented structures are produced, strongly reducing the material porosity.^{19, 22} Such nanostructure matched well with the results obtained.

The presence of a uniaxial hydrostatic pressure during the liquid phase sintering decisively influenced the orientation of the growing crystals. During the solution and reprecipitation step, the preferred orientation of the precipitating crystals is the one that minimizes chemical potential required for equilibrium across the plane normal to the pressure axis.²³ Such orientation depends on the elasticity of the material in each crystallographic direction, in such a way that in rather elastically anisotropic materials, such as $\text{Bi}_x\text{Sb}_{2-x}\text{Te}_3$, crystals align with the weakest crystallographic plane normal to the pressure axis. The layered structure of $\text{Bi}_x\text{Sb}_{2-x}\text{Te}_3$ crystals, with a strong bonding between atoms inside the ab plane and weak bonding between the layers in the c direction, results in a rather strong anisotropy of the elastic constants.²⁴ In particular, the Young modulus of Bi_2Te_3 crystals in the a and b axes are close to 30% larger than in the c axis.^{25, 26} Thus, during the liquid phase sintering under a uniaxial pressure, reprecipitated crystals would be oriented with the c direction parallel to the press axis, as we observed experimentally.

The presence of a uniaxial pressure during the liquid phase sintering may not only introduce a preferential orientation of the reprecipitated crystals, but it may also influence their geometry.^{23,}

²⁴ In the presence of a liquid phase able to partially dissolve and reprecipitate the crystals, the

uniaxial pressure promotes growth in its normal directions and aids the dissolution of the crystal in the directions parallel to this axis.^{23,24} In the particular case of $\text{Bi}_x\text{Sb}_{2-x}\text{Te}_3$, already in solution, at moderate temperatures and in the absence of a uniaxial pressure, nanocrystals grow faster in the ab plane than in the c -axis, thus acquiring flat, disk-shaped, morphologies. During the hot press process, the relative growth in the ab plane is much more accentuated and plates with much higher aspect ratios are finally obtained.

The initial shape of the pressed nanocrystals could influence the direction and even existence of a predominant orientation of the crystal domains in the final material.²⁷ Actually, in a previous work, no significant crystallographic texture was observed in pellets obtained from the hot press of ball milled $\text{Bi}_x\text{Sb}_{2-x}\text{Te}_3$ containing an excess of tellurium, even when using processing temperatures above the tellurium melting point.²⁸ To determine the role of the geometry of the precursor nanocrystal, we hot-pressed Bi_2Te_3 nanorods with the same excess of tellurium, $\text{Te}/\text{Bi} \sim 1.7$, and following the exact same steps as in the case of $\text{Bi}_x\text{Sb}_{2-x}\text{Te}_3$ nanodisks (Figure S8).²⁹ The polycrystalline material produced had a significant crystallographic texture ($I_{(0015)}/I_{(110)}=5.6$, Figure S9 and S10), but lower than that obtained with the $\text{Bi}_x\text{Sb}_{2-x}\text{Te}_3$ nanodisks ($I_{(0015)}/I_{(110)}=7.3$, Figure 2d). We also produced pellets by hot pressing a powder obtained from the ball milling of a commercial ingot and adding an excess of elemental tellurium to it. These pellets also showed some crystallographic alignment ($I_{(0015)}/I_{(110)}=3.1$, Figures S11 and S12), but also lower than the pellets produced from nanodisks (Figure 2d).

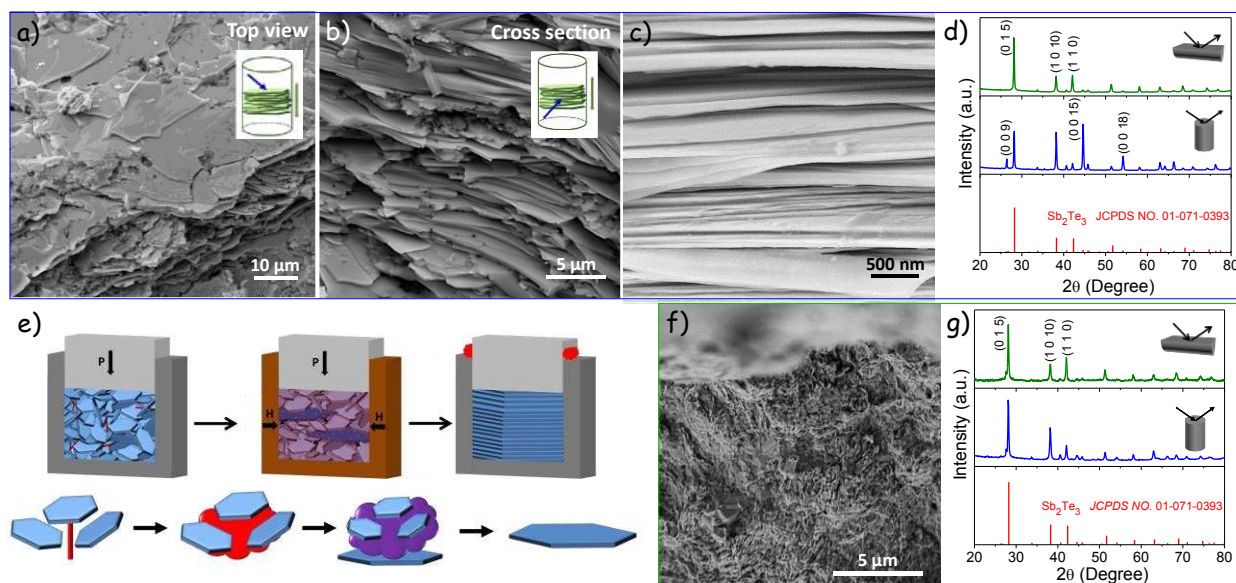


Figure 2. a) Top-view SEM micrograph of a $\text{Bi}_x\text{Sb}_{2-x}\text{Te}_3$ pellet produced at 480 °C. b) Cross-section SEM micrograph of the same pellet. c) Detail of the cross-section SEM micrograph. d) XRD patterns of the pellet placed to have the press axis within the diffraction plane (green) and normal to it (blue). e) Cartoon of the liquid-assisted sintering of the nanocrystals under uniaxial pressure. f) Cross-section SEM micrograph of a pellet hot-pressed at 300 °C. g) XRD patterns of the pellet hot-pressed at 300 °C placed to have the press axis within the diffraction plane (green) and normal to it (blue).

To produce consolidated nanomaterials with stoichiometric composition and having the finest crystallographic texture and optimum thermoelectric properties, it was essential to completely remove the excess amount of tellurium. Conveniently, during the hot press, while the temperature was above the tellurium melting point, the excess of this element was expelled through the plunger rod (Figure S13). However, in just one pressure and release step, the tellurium excess was not completely removed from the sample, probably due to the blocking of the scape paths within the layered structure or the plunger rod (Figure S14-S16). Only upon

multiple pressure and release steps the excess of tellurium could be totally ejected. Specifically, we used 5 pressure and release steps during the 210 s that the temperature was set at 480 °C to completely get rid of the tellurium excess. A similar cycling uniaxial pressure was previously reported to improve crystal alignment in spark plasma sintered $\text{Bi}_x\text{Sb}_{2-x}\text{Te}_3$, having no tellurium excess.¹⁸ No insight of the involved mechanism was reported in this previous work.

Among the different compositions tested, $\text{Bi}_{0.5}\text{Sb}_{1.5}\text{Te}_3$ provided the highest thermoelectric figures of merit (Figures S17-S20). We associated this experimental fact to a more optimum charge carrier concentration in this sample. This result is consistent with previous reports and with the use of this composition in commercial devices. Figure 3 shows the electrical conductivity, Seebeck coefficient, power factor, thermal conductivity, lattice thermal conductivity and overall thermoelectric figure of merit of the $\text{Bi}_{0.5}\text{Sb}_{1.5}\text{Te}_3$ nanomaterial hot pressed at 480 °C and measured in two directions, parallel and normal to the press axis (Figure S6). Displayed results were obtained from averaging experimental data from five different pellets (Figure S25 and S26). These results are compared in figure 3 with those obtained from a pellet produced with the exact same material, but hot pressed at a lower temperature, 300 °C, and a commercial ingot measured in the cleavage plane (*ab*) and its normal direction (*c*).

The nanomaterials hot pressed at 300 °C showed relatively low electrical conductivities (Figure 3a). Such low electrical conductivities were associated to a strong scattering of charge carriers at the ubiquitous grain interfaces of these materials. Additionally, these materials had lower relative densities than materials hot pressed at higher temperatures and contained an excess amount of tellurium which had not been expelled during the hot-press step.

On the other hand, nanomaterials hot-pressed at 480 °C showed very high electrical conductivities, comparable to those of the commercial sample. As expected, the electrical conductivities measured in the disk plane were higher than those obtained in the press direction ($\sigma_{ab}/\sigma_c = 1.6$ at 320 K). Such high electrical conductivities have been previously measured in samples processed in an excess of tellurium and were related to two main factors:^{27, 30} i) an increase (over materials with similar Bi/Sb ratios) of the hole concentration associated to a modification of the antisite and vacancy defects due to the tellurium excess;²⁹ ii) formation during the liquid phase sintering of semicoherent grain boundaries having a minimal effect on hole scattering.²⁷

Hall measurements of a series of five hot-pressed $\text{Bi}_{0.5}\text{Sb}_{1.5}\text{Te}_3$ nanomaterials measured three times showed the average charge carrier concentrations to be $p = 5 \pm 3 \times 10^{19} \text{ cm}^{-3}$, i.e. sensibly higher than that of the commercial material $p = 1.0 \pm 0.5 \times 10^{19} \text{ cm}^{-3}$. The mobilities measured in the plane normal to the press axis were on average a factor 1.6 higher than those measured in the press axis direction.

The Seebeck coefficients of the bottom-up assembled nanomaterials were significantly lower than those of the commercial sample, especially for the nanomaterial hot pressed at 480 °C (Figure 3b). These lower Seebeck coefficients were associated to the higher charge carrier concentrations present in the bottom-up nanomaterials. The higher charge carrier concentrations also explained that the Seebeck coefficients started to decrease at a higher temperature in the nanomaterial hot-pressed at 480 °C when compared with the commercial sample. On top of this retard of the bipolar effect associated to the higher charge carrier concentration, the excess of tellurium during the consolidation step could also reduce the density of tellurium vacancies, an

n-type defect, thus additionally decreasing the extent of the bipolar effect and shifting to even higher temperature the ZT maximum.

Seebeck coefficients measured in each of the two directions were very similar ($S_c/S_{ab} = 1.07$ at 320 K), as expected from the reduced anisotropy of this parameter already reported for single crystals ($S_c/S_{ab} = 1.02$).¹¹ Nevertheless, the coefficients measured in the press axis direction were slightly higher, which could point at some extend of selective scattering of the minority carriers at the crystal interfaces in the c direction.

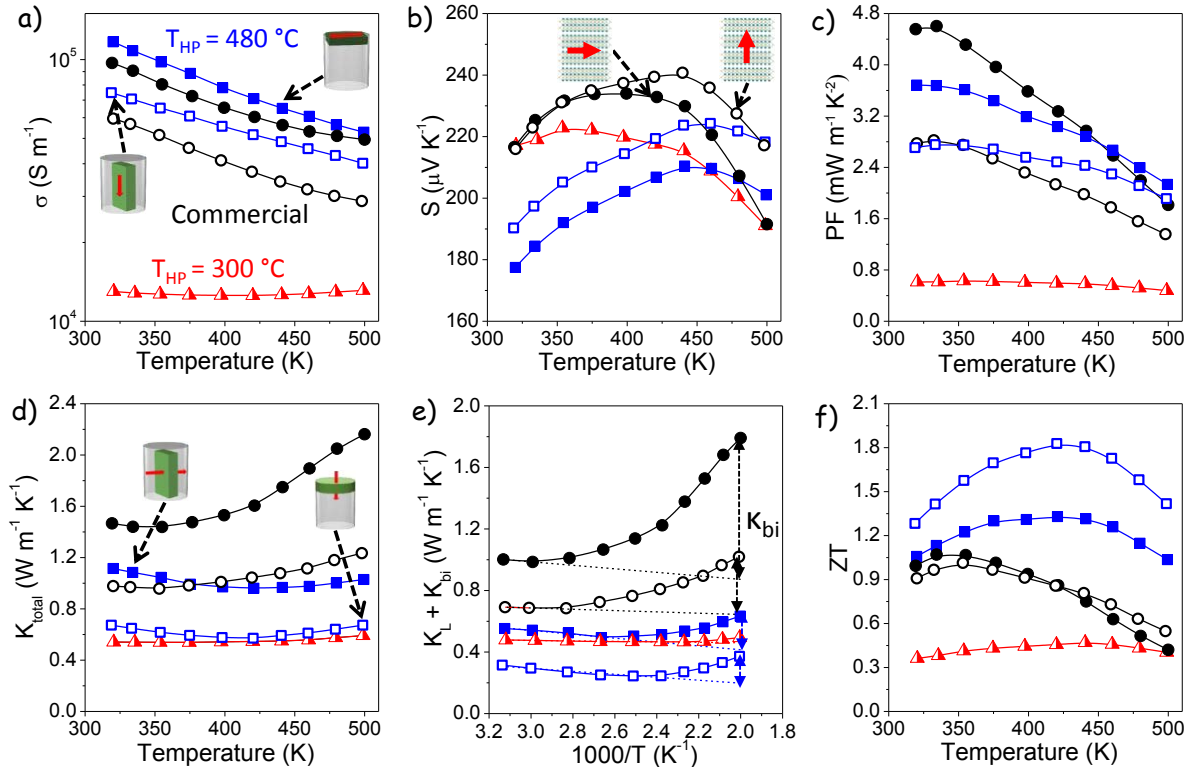


Figure 3. Thermoelectric properties of $\text{Bi}_{0.5}\text{Sb}_{1.5}\text{Te}_3$ nanomaterial hot pressed at 480 °C (blue squares) measured in two directions, parallel (open squares) and normal (solid squares) to the press axis (data were obtained from averaging the data values experimentally measured from 5 samples); $\text{Bi}_{0.5}\text{Sb}_{1.5}\text{Te}_3$ nanomaterial hot pressed at 300 °C (red triangles); and a commercial

ingot (black circles) measured in two directions, parallel (solid circles) and normal (open circles) to the cleavage direction. a) Electrical conductivity, σ ; b) Seebeck coefficient, S ; c) power factor, PF, d) thermal conductivity, κ ; e) lattice and bipolar thermal conductivity, $\kappa_L + \kappa_{bi} = \kappa_{total} - \kappa_e$; and f) thermoelectric figure of merit, ZT.

As expected, the thermal conductivities of the nanomaterials were significantly lower than those of the commercial sample, due to effective scattering at grain boundaries and crystal defects such as stacking faults (Figure 3d). For the nanomaterial hot pressed at 480 °C, the thermal conductivity was particularly low in the direction of the press axis ($\kappa_{ab}/\kappa_c = 1.64$ at 320 K), where a higher density of interfaces and stacking faults existed. In this direction, the thermal conductivity of this nanomaterial became comparable to that measured on the pellet hot pressed at 300 °C containing a random distribution of very small crystals. When taking into account the correction for the 10% porosity measured, i.e. a factor 1.33, the lowest lattice thermal conductivities that we measured at room temperature ($0.43 \text{ Wm}^{-1} \text{ K}^{-1}$) were slightly above the amorphous limit for Bi_2Te_3 ($0.31 \text{ Wm}^{-1} \text{ K}^{-1}$),³¹ and clearly above those estimated for highly defective Bi_2Te_3 (ca. $0.17 \text{ Wm}^{-1} \text{ K}^{-1}$),³² or for very small Bi_2Te_3 nanograins ($0.12 \text{ Wm}^{-1} \text{ K}^{-1}$)³³ and those measured for stacked Bi_2Te_3 2D films at room temperature ($0.1 \text{ Wm}^{-1} \text{ K}^{-1}$).³³

Thermal conductivities decreased with increasing temperature in the low temperature range and stabilized or increased in the high temperature range, when the bipolar contribution became significant (Figures 3e). Consistently with previous observations,³⁴ the bipolar contribution to the thermal conductivity was lower in the nanomaterial than in the commercial sample, which was attributed to a combination of the higher majority carrier concentration, the suppression of a source of minority carriers, such as tellurium vacancies, and the scattering of minority carriers at crystal interfaces or planar defects such as stacking faults.

Overall, the thermoelectric figures of merit ($ZT=S^2\sigma T/\kappa$) of the nanomaterial hot pressed at 480 °C were significantly higher than those of the commercial sample (Figure 3f). In particular, in the direction of the press axis, i.e. c , the combination of a high electrical conductivity, a notable Seebeck coefficient and a very low thermal conductivity resulted in thermoelectric figures of merit up to $ZT=1.96$ at 420 K for the record material and $ZT=1.83$ when averaged for 5 pellets. Dispersion of results provided from a dispersion of the charge carrier concentration in the samples. These values are the highest thermoelectric figure of merit reported in the ambient temperature range (Figure S22). Importantly, these high thermoelectric figures of merit were sustained in an extended temperature range. The average ZT , calculated over 180 K, from 320 K to 500 K, was $ZT_{ave}=1.77$ for the record material and $ZT_{ave}=1.65$ when averaging for 5 pellets. These values translated in potential energy conversion efficiencies up to 60% higher than those of commercial materials (SI).^{35, 36}

Notice that the figures of merit measured from the nanomaterial in the ab plane were systematically lower than those in the c direction (Figure 3f). This was somehow unexpected, since higher ZT values have been generally measured or assumed in the ab plane for single crystals and partially oriented polycrystalline materials.^{11, 15} The general assumption that the figures of merit in the ab plane must be higher than those in the c direction explain that in several previous works only the thermoelectric properties in the ab plane were measured, when possibly higher figures of merit would have been obtained in the normal direction.^{34, 37}

Finally, we want to highlight that the nanocrystalline $\text{Bi}_x\text{Sb}_{2-x}\text{Te}_3$ materials presented here showed good stability even when heated up to relatively high temperature (500 K) and during prolonged periods of time, as can be seen in figures S23-24.

Conclusions

We demonstrated the production of crystallographically textured $\text{Bi}_x\text{Sb}_{2-x}\text{Te}_3$ bulk nanomaterials with record thermoelectric figures of merit: $ZT=1.96$ for the record sample and $ZT=1.83$ when averaged over 5 materials at 420 K. These high ZT values also extended over a larger temperature range, resulting in ZT values averaged over 180 K as high as: $ZT_{\text{ave}}=1.77$ for the record material and $ZT_{\text{ave}}=1.65$ as the mean value from 5 samples. These unprecedented figures of merit were obtained in the c direction, in contrast with most previous works measuring or assuming better thermoelectric performances in the ab plane. Our procedure was based on several key parameters: i) the use of p-type $\text{Bi}_x\text{Sb}_{2-x}\text{Te}_3$ disk-shaped nanocrystals having controlled composition; b) the uniaxial hot press of the nanocrystals containing an excess of tellurium homogeneously distributed across the material; and c) the use of a proper hot press temperature and processing steps to ensure a proper liquid-assisted sintering and the complete removal of the tellurium excess.

ASSOCIATED CONTENT

Supporting information containing details of the chemicals used, NCs synthesis; pellet fabrication, materials characterization (X-ray diffraction patterns, SEM, electrical and thermal characterization); stability measurement and repeatability is available free of charge via the Internet at <http://pubs.acs.org>.

AUTHOR INFORMATION

Corresponding Author

* dycadavidr@unal.edu.co

*acabot@irec.cat

Author Contributions

The manuscript was prepared through the contribution of all authors. D. C. and A. C. guided the project, and supervised the work. Y. L., D. C., M.I., M.K. and A. C. conceived and prepared the manuscript. Y. L., S.O. and D. C. designed the experiments, produced the nanomaterials, and performed the thermoelectric characterization. Y. Z. and K. L. produced the bulk samples. M. I., K. L. and K. N. performed Hall measurement and analysed the results in this manuscript. A. G., S. M., and J. A. performed HRTEM and STEM-EELS and discussed these results. The manuscript was corrected and improved by all authors.

Notes

The authors declare no competing financial interest.

ACKNOWLEDGMENT

This work was supported by the European Regional Development Funds. YL and YZ thank the China Scholarship Council for scholarship support. M. V. K. acknowledges partial financial support by the European Union (EU) via FP7 ERC Starting Grant 2012 (Project NANOSOLID, GA No. 306733). SMS acknowledges funding from "Programa Internacional de Becas "la Caixa"-Severo Ochoa". IREC and ICN2 acknowledge funding from Generalitat de Catalunya 2014 SGR 1638. ICN2 acknowledges support from the Severo Ochoa Programme (MINECO, Grant no. SEV-2013-0295) and is funded by the CERCA Programme / Generalitat de Catalunya. Part of the present work has been performed in the framework of Universitat Autònoma de Barcelona Materials Science PhD program.

REFERENCES

1. Ortega, S.; Ibáñez, M.; Liu, Y.; Zhang, Y.; Kovalenko, M. V.; Cadavid, D.; Cabot, A. *Chem. Soc. Rev.* **2017**, 46, 3510-3528.
2. Zhu, T.; Hu, L.; Zhao, X.; He, J. *Adv. Sci.* **2016**, 3, 1600004.
3. Ibáñez, M.; Luo, Z.; Genç, A.; Piveteau, L.; Ortega, S.; Cadavid, D.; Dobrozhan, O.; Liu, Y.; Nachtegaal, M.; Zebarjadi, M. *Nat. Commun.* **2016**, 7, 10766.
4. Liu, Y.; Cadavid, D.; Ibáñez, M.; Ortega, S.; Martí-Sánchez, S.; Dobrozhan, O.; Kovalenko, M. V.; Arbiol, J.; Cabot, A. *APL Mater.* **2016**, 4, 104813.
5. Zebarjadi, M.; Joshi, G.; Zhu, G.; Yu, B.; Minnich, A.; Lan, Y.; Wang, X.; Dresselhaus, M.; Ren, Z.; Chen, G. *Nano Lett.* **2011**, 11, 2225-2230.
6. Ko, D.-K.; Kang, Y.; Murray, C. B. *Nano Lett.* **2011**, 11, 2841-2844.
7. Zhang, Q.; Ai, X.; Wang, L.; Chang, Y.; Luo, W.; Jiang, W.; Chen, L. *Adv. Funct. Mater.* **2015**, 25, 966-976.
8. Ibáñez, M.; Zamani, R.; Gorsse, S.; Fan, J.; Ortega, S.; Cadavid, D.; Morante, J. R.; Arbiol, J.; Cabot, A. *ACS nano* **2013**, 7, 2573-2586.
9. Ibáñez, M.; Korkosz, R. J.; Luo, Z.; Riba, P.; Cadavid, D.; Ortega, S.; Cabot, A.; Kanatzidis, M. G. *J. Am. Chem. Soc.* **2015**, 137, 4046-4049.
10. Liu, Y.; García, G.; Ortega, S.; Cadavid, D.; Palacios, P.; Lu, J.; Ibáñez, M.; Xi, L.; De Roo, J.; López, A.; Martí-Sánchez, S.; Cabezas, I.; Mata, M.; Luo, Z.; Dun, C.; Dobrozhan, O.; Carroll, D.; Zhang, W.; Martins, J.; Kovalenko, M.; Arbiol, J.; Noriega, G.; Song, J.; Wahnón, P.; Cabot, A. *J. Mater. Chem. A* **2017**, 5, 2592-2602.
11. Caillat, T.; Carle, M.; Pierrat, P.; Scherrer, H.; Scherrer, S. *J. Phys. Chem. Solids* **1992**, 53, 1121-1129.

12. Carle, M.; Pierrat, P.; Lahalle-Gravier, C.; Scherrer, S.; Scherrer, H. *J. Phys. Chem. Solids* **1995**, *56*, 201-209.
13. Kim, S.; Yamamoto, S.; Aizawa, T. *J. Alloys Compd.* **2004**, *375*, 107-113.
14. Fan, X.; Yang, J.; Zhu, W.; Bao, S.; Duan, X.; Xiao, C.; Li, K. *J. Alloys Compd.* **2008**, *461*, 9-13.
15. Santamaría, J. A.; Alkorta, J.; Sevillano, J. G. *J. Mater. Res.* **2015**, *30*, 2593-2604.
16. Yan, X.; Poudel, B.; Ma, Y.; Liu, W.; Joshi, G.; Wang, H.; Lan, Y.; Wang, D.; Chen, G.; Ren, Z. *Nano Lett.* **2010**, *10*, 3373-3378.
17. Han, L.; Spangsdorf, S. H.; Nong, N.; Hung, L.; Zhang, Y.; Pham, H. N.; Chen, Y.; Roch, A.; Stepien, L.; Pryds, N. *RSC Adv.* **2016**, *6*, 59565-59573.
18. Kitagawa, H.; Takimura, K.; Ido, S.; Morito, S.; Kikuchi, K. *J. Alloy. Comp.* **2017**, *692*, 388-394.
19. German, R. M., *Liquid phase sintering*. Springer Science & Business Media: **2013**.
20. Ghosh, G. *J. phase equilib.* **1994**, *15*, 349-360.
21. H. O. L. E. Tanner, *Phase Diagram*, ASM, **1986**.
22. Randall, M. G.; Pavan, S.; Seong, J. *J. Mater. Sci.* **2009**, *44*, 1-39.
23. Kamb, W. B. *J. Geol.* **1959**, *67*, 153-170.
24. Abdullaev, N. *Phys. Solid State* **2006**, *48*, 663-669.
25. Feng, S.; Li, S.; Fu, H. *Comput. Mater. Sci.* **2014**, *82*, 45-49.
26. Jenkins, J.; Rayne, J.; Ure Jr, R. *Phys. Rev. B* **1972**, *5*, 3171.
27. Paterson, M. *Rev. Geophys.* **1973**, *11*, 355-389.
28. Kim, S. I.; Lee, K. H.; Mun, H. A.; Kim, H. S.; Hwang, S. W.; Roh, J. W.; Yang, D. J.; Shin, W. H.; Li, X. S.; Lee, Y. H. *Science* **2015**, *348*, 109-114.

29. Zhang, G.; Kirk, B.; Jauregui, L. A.; Yang, H.; Xu, X.; Chen, Y. P.; Wu, Y. *Nano Lett.* **2011**, 12, 56-60.
30. Kim, Y. M.; Lydia, R.; Kim, J.-H.; Lin, C.-C.; Ahn, K.; Rhyee, J.-S. *Acta Mater.* **2017**, 135, 297-303.
31. Chiritescu, C.; Mortensen, C.; Cahill, D. G.; Johnson, D.; Zschack, P. *J. App. Phys.* **2009**, 106, (7), 073503.
32. Termentzidis, K.; Pokropyvnyy, O.; Woda, M.; Xiong, S.; Chumakov, Y.; Cortona, P.; Volz, S. *J. App. Phys.* **2013**, 113, (1), 013506.
33. Teweldebrhan, D.; Goyal, V.; Balandin, A. A. *Nano Lett.* **2010**, 10, (4), 1209-1218.
34. Zhang, C.; de la Mata, M.; Li, Z.; Belarre, F. J.; Arbiol, J.; Khor, K. A.; Poletti, D.; Zhu, B.; Yan, Q.; Xiong, Q. *Nano Energy* **2016**, 30, 630-638.
35. Kim, H. S.; Liu, W.; Chen, G.; Chu, C.-W.; Ren, Z. *Proc. Natl. Acad. Sci. U.S.A.* **2015**, 112, 8205-8210.
36. Kim, H. S.; Liu, W.; Ren, Z. *Energy Environ. Sci.* **2017**, 10, 69-85.
37. Park, K.; Ahn, K.; Cha, J.; Lee, S.; Chae, S. I.; Cho, S.-P.; Ryee, S.; Im, J.; Lee, J.; Park, S. *D. J. Am. Chem. Soc.* **2016**, 138, 14458-14468.

TOC graphical abstract

